

Chirality-Induced Spin Splitting in 1D InSeI

Shu Zhao,^{1,2,3} Jiaming Hu,^{2,3} Ziyu Zhu,^{2,3} Xiaoping Yao,^{2,3} and Wenbin Li^{2,3, a)}

¹⁾*School of Materials Science and Engineering, Zhejiang University, Hangzhou 310027, China*

²⁾*Key Laboratory of 3D Micro/Nano Fabrication and Characterization of Zhejiang Province, School of Engineering, Westlake University, Hangzhou 310030, China*

³⁾*Institute of Advanced Technology, Westlake Institute for Advanced Study, Hangzhou 310024, China*

(Dated: 13 October 2023)

Spin-orbit coupling in chiral materials can induce chirality-dependent spin splitting, enabling electrical manipulation of spin polarization. Here, we use first-principles calculations to investigate the electronic states of chiral one-dimensional (1D) semiconductor InSeI, which has two enantiomorphic configurations with left- and right-handedness. We find that opposite spin states exist in the left- and right-handed 1D InSeI with significant spin splitting and spin-momentum collinear locking. Although the spin states at the conduction band minimum (CBM) and valence band maximum (VBM) of 1D InSeI are both nearly degenerate, a direct-to-indirect bandgap transition occurs when a moderate tensile strain ($\sim 4\%$) is applied along the 1D chain direction, leading to a sizable spin splitting (~ 0.11 eV) at the CBM. These findings indicate that 1D InSeI is a promising material for chiral spintronics.

Chirality extensively exists in nature, originating from a symmetry breaking where an object cannot superimpose itself through reflection or inversion operations¹⁻⁴. Chiral materials exhibit a wide range of fascinating properties, including magneto-chiral dichroism⁵, non-reciprocal transport⁶, and novel topological quantum phenomena⁷. In particular, chiral materials could be promising candidates for spintronic devices, since their chirality-dependent spin splitting allows the electrical manipulation of spin polarization^{4,8-12}. However, the development of chirality-based spintronics is currently dominated by organic and hybrid organic-inorganic materials^{4,13}. Despite the discovery of some intriguing phenomena in these chiral materials such as chirality-induced spin selectivity¹³, the lack of inorganic materials with chirality¹⁰⁻¹² still hinders the utilization of chiral spintronic devices.

Bulk indium selenoiodide (InSeI) has a quasi-one-dimensional structure consisting of both left- and right-handed chiral nanochains, as illustrated in Figure 1a. The synthesis of bulk InSeI and its crystal structure analysis was first reported by Sawitzki et al. in 1980¹⁴. Recently, one-dimensional (1D) nanochains of InSeI were separated from their bulk counterpart by micromechanical exfoliation¹⁵, further enabling the studies of 1D InSeI. In addition to these experimental advances, theoretical calculations reveal that 1D InSeI exhibits a large direct bandgap (~ 3.15 eV) and a moderate electron effective mass ($\sim 0.49 m_0$)¹⁶, indicating the potential of 1D InSeI for nanoelectronic and optoelectronic applications. However, the effect of chirality on the electronic structure of 1D InSeI is still underappreciated.

In this work, through density functional theory (DFT) calculations, we investigate the electronic and spin states

of chiral 1D InSeI with left- and right-handedness. Importantly, the band structure of 1D InSeI exhibits significant spin splitting due to the inversion symmetry breaking of the chiral structure. Although the spin states (containing spin up and spin down) are nearly degenerate at the conduction band minimum (CBM) and valence band maximum (VBM), a sizable spin splitting (~ 0.11 eV) could be present at the CBM by applying a moderate amount ($\sim 4\%$) of tensile strain. The large spin splitting at the CBM suggests that spin-polarized current with chirality dependence could be electrically generated in the strained 1D InSeI. Therefore, our work not only elucidates the effect of chirality on the electronic structure of 1D InSeI, but also demonstrates the potential of 1D InSeI for chiral spintronics.

The calculations of the electronic states in 1D InSeI are performed by DFT as implemented in the VASP code¹⁷, using the projector augmented-wave (PAW) method^{18,19} and the Perdew-Burke-Ernzerhof (PBE) exchange-correlation functional²⁰. Setting the z axis along the chain direction, a vacuum thickness of 15 Å across xy -plane is included to avoid the spurious interaction between the helical chain and its periodic images. A plane-wave cutoff energy of 500 eV and $1 \times 1 \times 12$ grids of \mathbf{k} -points are employed, which are sufficient to converge the total energy within 3 meV per atom. The unit-cell dimension along the z -axis and the atomic positions are fully relaxed until the energy is converged to within 10^{-6} eV and the maximum forces on each atom are less than 0.001 eV/Å.

The crystal structure of 1D InSeI belongs to the $P4_1$ (No. 76) space group and exhibits two helical enantiomorphic configurations with left- and right-handedness, as shown in Figure 1b. The corner-sharing I-In-Se tetrahedra are connected to form a helical structure along the c axis. Each Se atom is shared by three tetrahedra and within each tetrahedra, one In atom links with one I atom and three Se atoms. The In-Se bond length as obtained

^{a)}Electronic mail: liwenbin@westlake.edu.cn

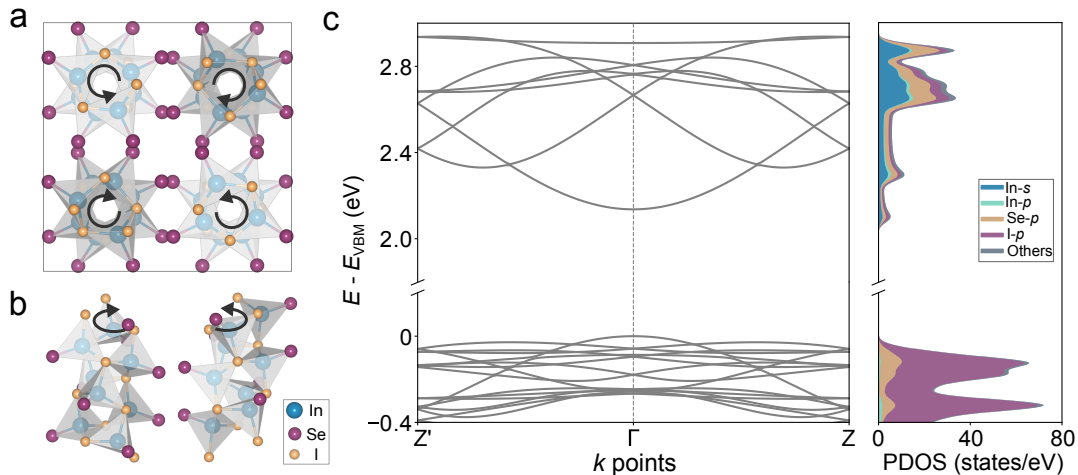


FIG. 1. Crystal and electronic structures of InSeI. (a) The crystal structure of bulk InSeI contains two types (left-handed and right-handed) of chiral chains. (b) Crystal structures of left- and right-handed 1D InSeI. Blue, yellow, and purple balls represent In, Se, and I atoms, respectively. (c) Electronic band structure and projected density of states (PDOS) of the 1D InSeI without the inclusion of spin-orbit coupling (SOC), as calculated by density functional theory (DFT).

from DFT calculations is measured to be in the range of 2.65 to 2.7 Å, while the In-I bond length is 2.7 Å (see **Figure S1**). Each unit cell of the 1D InSeI nanochain contains 24 atoms (8 formula units), and the fully-relaxed unit-cell dimension along the z -axis is 10.4 Å.

We start the investigation of the electronic states of 1D InSeI by carrying out band structure calculations without the inclusion of spin-orbit coupling (SOC). As illustrated in Figure 1c, the conduction band minimum (CBM) and valence band maximum (VBM) of 1D InSeI are both located at the Γ point with a DFT-PBE bandgap of 2.14 eV. Using the more accurate HSE06 functional²¹, the calculated bandgap of 1D InSeI is 3.06 eV (see **Figure S2**), which is larger than those of most other reported 1D semiconductor materials^{22–24}. From the right panel of Figure 1c, it can be seen that the conduction bands (CBs) of 1D InSeI has a significant contribution from the In- s and In- p orbitals, whereas the valence bands (VBs) are dominated by the contributions from the Se- p and I- p orbitals.

Given that the chiral 1D InSeI nanochains do not possess inversion symmetry, SOC could have a significant influence on their electronic structures. Hence, we next calculate the electronic states of 1D InSeI with the SOC effect included, as well as investigating their chirality dependence. The comparison of the band structures of 1D InSeI with and without SOC is shown in Figure 2a, with the zoom-in views in the vicinity of the valence and conduction band edges shown in **Figure S3**. The results indicate that 1D InSeI has a similar direct bandgap at the Γ point regardless of the inclusion of the SOC effect (1.96 eV with SOC and 2.14 eV without SOC). Although the effect of SOC on the bandgap is insignificant, it leads to evident band splittings in both the CBs and the VBs. Intriguing, certain CBs exhibit much stronger spin splitting than the others. This is because SOC requires non-

zero orbital angular momentum, and the CB states with a larger In- p orbital contribution have a stronger spin splitting than those with the In- s orbital contribution, as indicated by the k -resolved projected density of states in **Figure S4**.

With the inclusion of SOC effect, the 1D InSeI nanochains remain non-magnetic and the calculated net atomic magnetic moments of In, Se, and I atoms are all zero. However, the individual electronic states can exhibit non-zero spin expectation values due to the spin splitting caused by SOC. We thus calculate the expectation values of the spin operators (S_x , S_y , and S_z) on the electronic states of left- and right-handed 1D InSeI. The results in **Figure S5** show that only $\langle S_z \rangle$ has non-zero contribution to the spin polarization of the electronic states, indicating that polarized spins are aligned along the chain direction ($\pm k_z$ direction) in 1D InSeI. Such spin-momentum collinear locking is a hallmark of the spin polarization in chiral materials with helical structures^{12,25}.

The band structures with the $\langle S_z \rangle$ values of left- and right-handed 1D InSeI are plotted in Figure 2b,c. We can see that left- and right-handed 1D InSeI exhibit opposite spin characteristics at the same wavevector and band index, demonstrating chirality-dependent spin splitting. However, the VBM and CBM of 1D InSeI are located very close to the Γ point (see **Figure S6**), where spin degeneracy is enforced by Kramers' theorem²⁶. The rather small spin splitting at the CBM and VBM could introduce difficulty for the generation and detection of spin-polarized current in spintronic devices. In addition, the calculated energy difference between the vacuum level and the VBM is rather large (6.66 eV), exceeding the largest metallic work function (~ 5.65 eV for platinum²⁷). The mismatch in work function would make it difficult to form Ohmic contact with hole-conducting InSeI in prac-

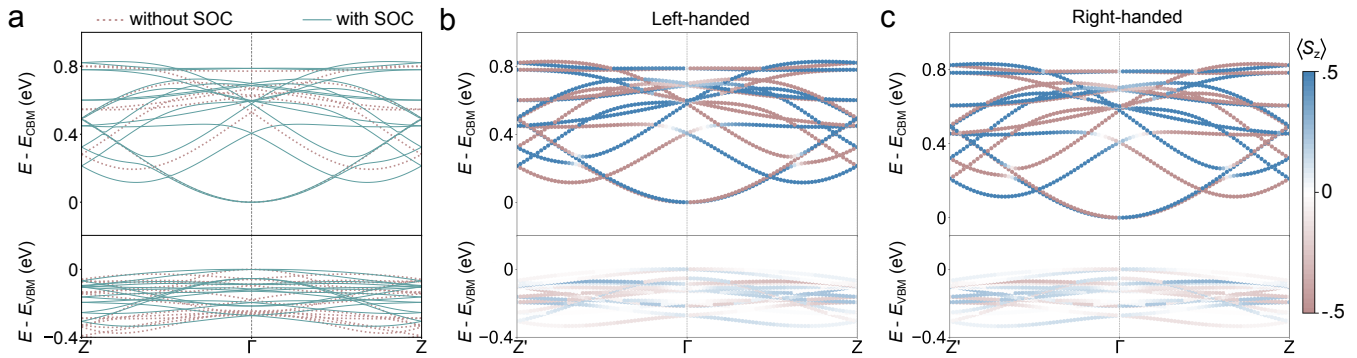


FIG. 2. Chirality-dependent spin splitting of 1D InSe. (a) Comparison of the calculated electronic band structures of a InSe nanochain with (green lines) and without (red dotted lines) the inclusion of SOC. (b,c) Calculated band structures of left-handed (b) and right-handed (c) InSe nanochains with the expectation values of the spin operator S_z on the spinor wave functions. The unit of the expectation value $\langle S_z \rangle$ is \hbar .

tical devices. In fact, according to the “doping limit rule” of wide bandgap semiconductors, the deep VBM level of 1D InSe indicates that its p -type doping would be difficult to realize²⁸. In comparison, the calculated energy difference between the vacuum level and the CBM has a much smaller value of 4.52 eV. Therefore, in the following discussion, we focus on how to induce a spin-splitting at the CBM much larger than the thermal energy (~ 26 meV) at room temperature, which would be needed for room-temperature spintronic applications.

Strain engineering has played an important role in controlling the electronic properties of nanostructured materials^{29–31}, such as the significant strain modulation of the electronic bandgaps of 2D and 1D chalcogenides^{32–34}. Indeed, tensile strain can increase the distance between adjacent atomic sites in a crystal, resulting in smaller electron hopping energies and thus smaller electron bonding-antibonding splittings. This causes the energy level of an anti-bonding orbital to move downward and that of a bonding orbital to move upward, leading to changes in the electronic properties of materials. From the crystal structure of 1D InSe (see Figure 1a,b), it can be seen that the In atoms and Se atoms bond together to form the skeleton of the helical chain, while the In-I bonds are almost perpendicular to the helical skeleton. Therefore, the energy levels of the CBs with a stronger In-Se bonding or antibonding character is expected to be more susceptible to tensile strain applied along the chain direction.

Figure 3a depicts the wavevector-dependent crystal orbital Hamilton population (COHP) of the In-Se bond for the electronic states in the CBs of 1D InSe, calculated using the LOBSTER code^{35,36}. It can be seen that the band-energy local minimum between Γ and Z/Z' , denoted by D/D' , has a stronger In-Se anti-bonding interaction than that of the CBM at the Γ point. In addition, the partial charge densities of the CBM at Γ and D/D' are calculated to visualize their wavefunctions. We can see that, for the local band minima at D/D' , almost all

the charge densities are distributed around the In and Se atoms. For the CBM at Γ point, however, significant charges surround the I atoms. Taken the COHP and wavefunction information together, when a tensile strain is applied along the chain direction, the energy of the band minimum at D/D' is expected to be more sensitive to the tensile strain than that at the Γ . This will contribute to a steeper downward shift of CBM at the D/D' than that at the Γ point.

To further quantify the band energy changes, the DFT-calculated CBM levels of a InSe nanochain as a function of tensile strain (with the inclusion of SOC) is shown in Figure 3c. Under the applied tensile strains, which vary from 0 to 8% at a step of 2%, the energy of the CBM at D/D' has a faster rate of decrease than that at Γ . Once the tensile strain imposed on 1D InSe is larger than $\sim 4\%$, the energy level of the CBM at D/D' becomes lower than that of the CBM at Γ , resulting in a direct-to-indirect bandgap transition (detailed strain-dependent band structures are shown in **Figure S7**). When the transition occurs, a significant chirality-dependent spin-splitting (~ 0.11 eV) emerges at the CBM, as illustrated in Figure 3(d,e). The spin polarization of the bands along the high-symmetry paths $\Gamma - Z$ and $\Gamma - Z'$ are opposite in left- and right-handed 1D InSe.

We have further considered the effect of electrostatic carrier doping on the electronic structure and strain-induced band structural change in 1D InSe, given that in practical devices, a finite amount of charge carriers is present in the system. The effect of electrostatic doping is modeled using the background charge approach, with fully relaxed atomic positions. When the electron doping concentration (n_e) of 1D InSe is 0.01 electron per formula unit ($e/f.u.$), corresponding to $n_e \approx 1.1 \times 10^{20} \text{ cm}^{-3}$, a number approaching the maximum electron doping concentration of n -type silicon³⁷, the change in its electronic structure is negligible, as shown in **Figure S8a**. In particular, an external tensile strain of $\sim 4\%$ can still cause the CBM at D/D' to become lower in energy than

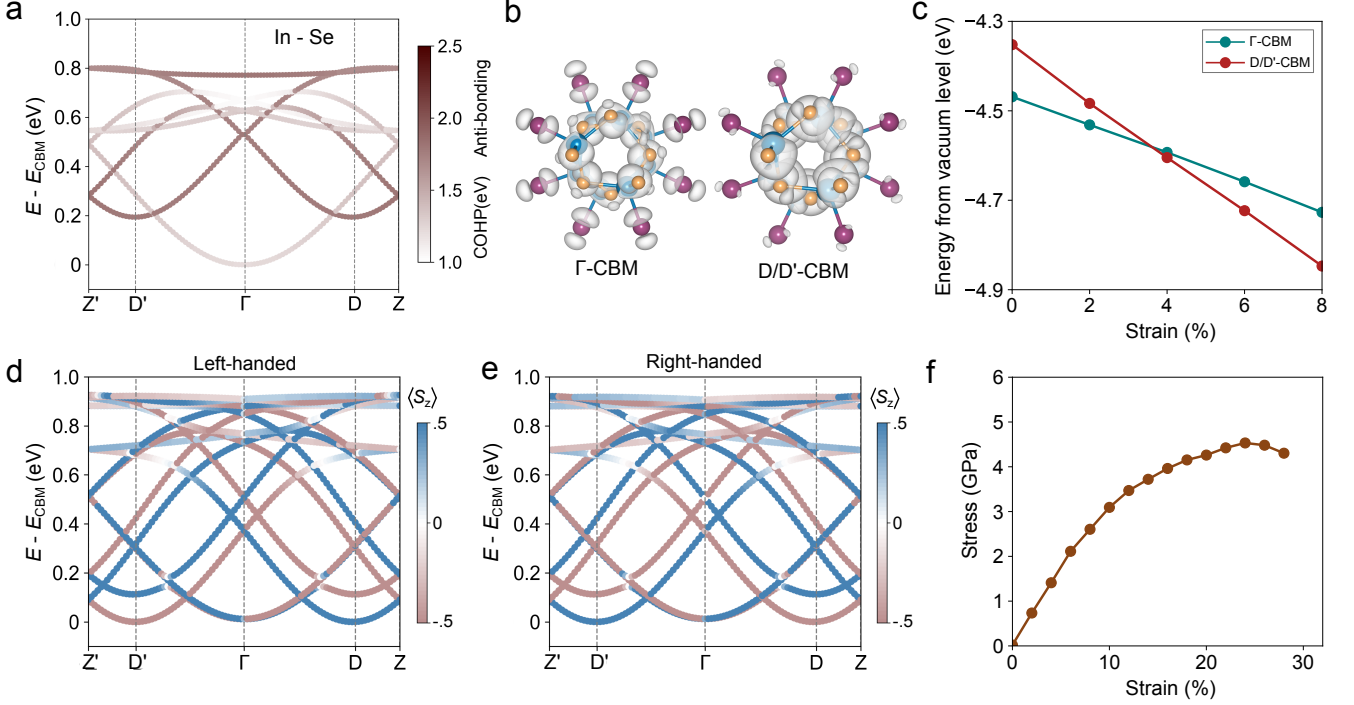


FIG. 3. Strain-modulated electronic states in 1D InSeI. (a) State-resolved crystal orbital Hamilton population (COHP) of the In-Se bonds for the conduction-band electronic states. The band structure without the SOC effect is used for the analysis. (b) Partial charge densities of the conduction band minimum (CBM) at the high-symmetry points Γ and D/D' . (c) Strain-dependent CBM levels at Γ and D/D' with the inclusion of SOC. (d,e) Calculated band structures with the $\langle S_z \rangle$ values on the electronic states of left- (d) and right-handed (e) 1D InSeI under a tensile strain of 4%. (f) DFT-calculated intrinsic stress-strain curve of 1D InSeI.

the CBM at Γ in the electron-doped 1D InSeI, as illustrated in **Figure S8b**. The result is therefore essentially the same as that of 1D InSeI without the inclusion of additional electrons. Thus, we conclude that the perturbation of the electrostatic doping on the strain-induced band structural evolution of 1D InSeI is insignificant.

Although spin splitting occurs at the CBM by applying a $\sim 4\%$ tensile strain, it is unclear whether 1D InSeI can withstand the level of tensile strain. Thus, we next explore the intrinsic mechanical properties of 1D InSeI. By applying tensile strains along the chain direction from -1% to 1% with a step of 0.2% , the Young's modulus (Y) of 1D InSeI is calculated using the formula $Y = V_0^{-1} \partial^2 E / \partial \epsilon^2$, where E is the system energy under strain ϵ . The equilibrium volume V_0 is given by $V_0 = \pi r^2 L$, where L and r denote the length along the z axis (chain direction) and the radius of 1D InSeI in the xy plane as measured from the iodine atoms, respectively.

The calculated Young's modulus of 1D InSeI is ~ 34 GPa, which is much smaller than the average Young's modulus of carbon nanotubes (1.8 TPa)³⁸. The small stiffness of 1D InSeI suggests the potential for flexible semiconductor devices. Furthermore, we calculate the strain-stress curve of 1D InSeI, as shown in **Figure 3f**. The stress (σ) of the 1D InSeI is measured using the formula³⁹ $\sigma = \sigma_0 S_0 / S$, where S_0 and S are the cross section

(xy plane) areas with and without the inclusion of vacuum layer, respectively. σ_0 is the stress along the chain direction (z axis) from direct DFT output.

The critical stress and strain corresponding to mechanical failure as determined from the stress-strain curve are 4.7 GPa and 24% , respectively. The intrinsic mechanical failure strain is greater than the strain at which the indirect-to-direct bandgap transition occurs. Apart from the mechanical stability, we also investigate the dynamical and thermal stability of 1D InSeI under mechanical strain. The phonon spectrum of 1D InSeI under a tensile strain of 5% , calculated using the force-constant approach implemented in the PHONOPY code⁴⁰, is shown in **Figure S9**. The absence of an imaginary phonon mode indicates the dynamical stability of 1D InSeI under a tensile strain of 5% . In addition, *ab initio* molecular dynamics (AIMD) simulation of 1D InSeI under a strain of 5% at 350 K is performed using a $1 \times 1 \times 3$ supercell, with a total simulation length of 5 ps at a timestep of 1 fs. **Figure S10** shows that the helical framework and the atomic bonds of 1D InSeI are well preserved during the AIMD run, indicating its thermal stability. Additional calculations of the COHP and integrated COHP (ICOHP) values of 1D InSeI as a function of the applied tensile strain are shown in **Figure S1**. All the calculation results confirm that 1D InSeI maintains mechanical,

dynamical, thermal, and bonding stability under a tensile strain of at least 5%, which is higher than the critical strain of 4% to induce the direct-to-indirect bandgap transition and strong spin-splitting at the CBM. Experimentally, it has been demonstrated that silicon nanowires with diameters of ~ 100 nm can be repeatedly stretched above 10% elastic strain at room temperature⁴¹, indicating that experimental realization of the strain-induced electronic structural changes in 1D InSeI is entirely feasible. These properties make 1D InSeI a useful materials system for mechano-spintronic applications, where tensile strain could modulate the spin polarization of the electrical current passing through the chiral 1D material.

In summary, through first-principles calculations and analysis, we study the effect of chirality on the electronic states of 1D InSeI. We find that spin-orbit coupling in the chiral 1D semiconductor induces chirality-dependent spin splitting and spin-momentum collinear locking in the conduction and valence bands. By applying an external tensile strain of $\sim 4\%$ along the 1D chain direction, a large spin splitting of 0.11 eV emerges at the CBM along with a direct-to-indirect bandgap transition. These results highlight the potential of 1D InSeI for chiral spintronic and mechano-spintronic applications.

We gratefully acknowledge the support by NSFC under Project No. 62004172. The work of W.L. is partially supported by Research Center for Industries of the Future at Westlake University under Award No. WU2022C041. The authors thank Drs. J.-Q. Wang and C. Hu for helpful discussions and the HPC Center of Westlake University for technical assistance.

I. SUPPLEMENTARY MATERIAL

Calculations of the COHP and ICOHP of 1D InSeI; band structures of 1D InSeI under different tensile strains along the chain direction; spin expectation values of the electronic states in 1D InSeI; the effects of electron doping on the electronic structure of 1D InSeI; phonon spectrum and AIMD simulation of 1D InSeI under 5% tensile strain.

- ¹H. D. Flack, "Chiral and achiral crystal structures," *Helv. Chim. Acta* **86**, 905–921 (2003).
- ²G. H. Fecher, J. Kübler, and C. Felser, "Chirality in the solid state: chiral crystal structures in chiral and achiral space groups," *Materials* **15**, 5812 (2022).
- ³G. Long, R. Sabatini, M. I. Saidaminov, G. Lakhwani, A. Rasmita, X. Liu, E. H. Sargent, and W. Gao, "Chiral-perovskite optoelectronics," *Nat. Rev. Mater.* **5**, 423–439 (2020).
- ⁴S.-H. Yang, R. Naaman, Y. Paltiel, and S. S. P. Parkin, "Chiral spintronics," *Nat. Rev. Phys.* **3**, 328–343 (2021).
- ⁵C. Train, R. Gheorghe, V. Krstic, L.-M. Chamoreau, N. S. Ovanesyan, G. L. J. A. Rikken, M. Gruselle, and M. Verdaguer, "Strong magneto-chiral dichroism in enantiopure chiral ferromagnets," *Nat. Mater.* **7**, 729–734 (2008).
- ⁶Y. Tokura and N. Nagaosa, "Nonreciprocal responses from non-centrosymmetric quantum materials," *Nat. Commun.* **9**, 3740 (2018).
- ⁷G. Chang, B. J. Wieder, F. Schindler, D. S. Sanchez, I. Belopolski, S.-M. Huang, B. Singh, D. Wu, T.-R. Chang, T. Neupert,

- S.-Y. Xu, H. Lin, and M. Z. Hasan, "Topological quantum properties of chiral crystals," *Nat. Mater.* **17**, 978–985 (2018).
- ⁸G. L. J. A. Rikken, J. Fölling, and P. Wyder, "Electrical magnetochiral anisotropy," *Phys. Rev. Lett.* **87**, 236602 (2001).
- ⁹T. Yoda, T. Yokoyama, and S. Murakami, "Current-induced orbital and spin magnetizations in crystals with helical structure," *Sci. Rep.* **5**, 12024 (2015).
- ¹⁰A. Inui, R. Aoki, Y. Nishiue, K. Shiota, Y. Kousaka, H. Shishido, D. Hirobe, M. Suda, J.-i. Ohe, J.-i. Kishine, H. M. Yamamoto, and Y. Togawa, "Chirality-induced spin-polarized state of a chiral crystal CrNb₃S₆," *Phys. Rev. Lett.* **124**, 166602 (2020).
- ¹¹K. Shiota, A. Inui, Y. Hosaka, R. Amano, Y. Ōnuki, M. Hedo, T. Nakama, D. Hirobe, J.-i. Ohe, J.-i. Kishine, H. M. Yamamoto, H. Shishido, and Y. Togawa, "Chirality-induced spin polarization over macroscopic distances in chiral disilicide crystals," *Phys. Rev. Lett.* **127**, 126602 (2021).
- ¹²F. Calavalle, M. Suárez-Rodríguez, B. Martín-García, A. Johansson, D. C. Vaz, H. Yang, I. V. Maznichenko, S. Ostanin, A. Mateo-Alonso, A. Chuvilin, I. Mertig, M. Gobbi, F. Casanova, and L. E. Hueso, "Gate-tuneable and chirality-dependent charge-to-spin conversion in tellurium nanowires," *Nat. Mater.* **21**, 526–532 (2022).
- ¹³R. Naaman, Y. Paltiel, and D. H. Waldeck, "Chiral molecules and the electron spin," *Nat. Rev. Chem.* **3**, 250–260 (2019).
- ¹⁴G. Sawitzki, D. Müller, and H. Hahn, "Die kristallstrukturen von InTeI und InSeI," *Mater. Res. Bull.* **15**, 753–762 (1980).
- ¹⁵K. H. Choi, S. Cho, B. J. Jeong, B. Lee, J. Jeon, J. Kang, X. Zhang, H.-S. Oh, J.-H. Lee, H. K. Yu, and J.-Y. Choi, "One-dimensional van der Waals material InSeI with large band-gap for optoelectronic applications," *J. Alloys Compd.* **927**, 166995 (2022).
- ¹⁶S. Jiang, H. Yin, G.-P. Zheng, B. Wang, S. Guan, and B.-J. Yao, "Computational prediction of a novel 1D InSeI nanochain with high stability and promising wide-bandgap properties," *Phys. Chem. Chem. Phys.* **22**, 27441–27449 (2020).
- ¹⁷G. Kresse and J. Furthmüller, "Efficient iterative schemes for *ab initio* total-energy calculations using a plane-wave basis set," *Phys. Rev. B* **54**, 11169–11186 (1996).
- ¹⁸P. E. Blöchl, "Projector augmented-wave method," *Phys. Rev. B* **50**, 17953–17979 (1994).
- ¹⁹G. Kresse and D. Joubert, "From ultrasoft pseudopotentials to the projector augmented-wave method," *Phys. Rev. B* **59**, 1758–1775 (1999).
- ²⁰J. P. Perdew, K. Burke, and M. Ernzerhof, "Generalized gradient approximation made simple," *Phys. Rev. Lett.* **77**, 3865 (1996).
- ²¹J. Heyd, G. E. Scuseria, and M. Ernzerhof, "Hybrid functionals based on a screened Coulomb potential," *J. Chem. Phys.* **118**, 8207–8215 (2003).
- ²²B. Peng, K. Xu, H. Zhang, Z. Ning, H. Shao, G. Ni, J. Li, Y. Zhu, H. Zhu, and C. M. Soukoulis, "1D SbSeI, SbSI, and SbSBr with high stability and novel properties for microelectronic, optoelectronic, and thermoelectric applications," *Adv. Theory Simul.* **1**, 1700005 (2018).
- ²³D. Pfister, K. Schäfer, C. Ott, and et al., "Inorganic double helices in semiconducting SnIP," *Adv. Mater.* **28**, 9783–9791 (2016).
- ²⁴S. Zhao, C. Yang, Z. Zhu, X. Yao, and W. Li, "Curvature-controlled band alignment transition in 1D van der Waals heterostructures," *npj Comput. Mater.* **9**, 92 (2023).
- ²⁵S.-H. Yang, "Chirality tweaks spins in tellurium," *Nat. Mater.* **21**, 494–495 (2022).
- ²⁶M. Lax, *Symmetry Principles in Solid State and Molecular Physics* (Wiley, New York., 1974).
- ²⁷H. B. Michaelson, "The work function of the elements and its periodicity," *J. Appl. Phys.* **48**, 4729–4733 (1977).
- ²⁸S. B. Zhang, S.-H. Wei, and A. Zunger, "A phenomenological model for systematization and prediction of doping limits in II-VI and I-III-VI₂ compounds," *J. Appl. Phys.* **83**, 3192–3196 (1998).
- ²⁹T. Zhu and J. Li, "Ultra-strength materials," *Prog. Mater. Sci.* **55**, 710–757 (2010).

- ³⁰J. Li, Z. Shan, and E. Ma, "Elastic strain engineering for unprecedented materials properties," *MRS Bull.* **39**, 108–114 (2014).
- ³¹J. Li, "EML webinar overview: elastic strain engineering for unprecedented properties," *Extreme Mech. Lett.* **54**, 101430 (2022).
- ³²J. Feng, X. Qian, C.-W. Huang, and J. Li, "Strain-engineered artificial atom as a broad-spectrum solar energy funnel," *Nat. Photonics* **6**, 866–872 (2012).
- ³³P. Johari and V. B. Shenoy, "Tuning the electronic properties of semiconducting transition metal dichalcogenides by applying mechanical strains," *ACS Nano* **6**, 5449–5456 (2012).
- ³⁴W. Li, G. Zhang, M. Guo, and Y.-W. Zhang, "Strain-tunable electronic and transport properties of MoS₂ nanotubes," *Nano Res.* **7**, 518–527 (2014).
- ³⁵S. Maintz, V. L. Deringer, A. L. Tchougréeff, and R. Dronskowski, "LOBSTER: a tool to extract chemical bonding from plane-wave based DFT," *J. Comput. Chem.* **37**, 1030–1035 (2016).
- ³⁶U. Häussermann, P. Berastegui, S. Carlson, J. Haines, and J.-M. Léger, "TiF and PbO under high pressure: unexpected persistence of the stereochemically active electron pair," *Angew. Chem. Int. Ed.* **40**, 4624–4629 (2001).
- ³⁷J. Dziewior and W. Schmid, "Auger coefficients for highly doped and highly excited silicon," *Appl. Phys. Lett.* **31**, 346–348 (1977).
- ³⁸M. M. J. Treacy, T. W. Ebbesen, and J. M. Gibson, "Exceptionally high young's modulus observed for individual carbon nanotubes," *Nature* **381**, 678–680 (1996).
- ³⁹C. Shang, L. Fu, S. Zhou, and J. Zhao, "Atomic wires of transition metal chalcogenides: a family of 1D materials for flexible electronics and spintronics," *JACS Au* **1**, 147–155 (2020).
- ⁴⁰A. Togo and I. Tanaka, "First principles phonon calculations in materials science," *Scr. Mater.* **108**, 1–5 (2015).
- ⁴¹H. Zhang, J. Tersoff, S. Xu, H. Chen, Q. Zhang, K. Zhang, Y. Yang, C.-S. Lee, K.-N. Tu, J. Li, and Y. Lu, "Approaching the ideal elastic strain limit in silicon nanowires," *Sci. Adv.* **2**, e150138 (2016).